Interactions of relativistic neon to nickel projectiles in hydrogen, elemental production cross sections

C. N. Knott,[6] S. Albergo,[4] Z. Caccia,[4] C.-X. Chen,[1] S. Costa,[4] H. J. Crawford,[2] M. Cronqvist,[2] J. Engelage,[2] P. Ferrando,[3] R. Fonte,[4] L. Greiner,[2] T. G. Guzik,[1] A. Insolia,[4] F. C. Jones,[5] P. J. Lindstrom,[7] J. W. Mitchell,[5] R. Potenza,[4] J. Romanski,[7,4] G. V. Russo,[4] A. Soutoul,[3] O. Testard,[3] C. E. Tull,[1,*] C. Tuvé,[4] C. J. Waddington,[6] W. R. Webber,[8] and J. P. Wefel[1]

(Transport Collaboration)

[1]*Department of Physics and Astronomy, Louisiana State University, Baton Rouge, Louisiana 70803*

[2]*Space Science Laboratory, University of California, Berkeley, California 94720*

[3]*Service d'Astrophysique, Centre d'Etudes Nucléaires–Saclay, 91191 Gif-sur-Yvette, Cedex, France*

[4]*Dipartimento di Fisica, Universitá di Catania and INFN-Sezione di Catania, Corso Italia 57, I 95129 Catania, Italy*

[5]*NASA/Goddard Space Flight Center, Greenbelt, Maryland 20771*

[6]*School of Physics and Astronomy, University of Minnesota, Minneapolis, Minnesota 55455*

[7]*Lawrence Berkeley Laboratory, 1 Cyclotron Road, Berkeley, California 94720*

[8]*Department of Astronomy, New Mexico State University, Las Cruces, New Mexico 88003*

(Received 3 August 1995)

This paper reports the elemental production cross sections for 17 projectile-energy combinations with energies between 338 and 894 MeV/nucleon interacting in a liquid hydrogen target. These results were obtained from two runs at the LBL Bevalac using projectiles ranging from ^{22}Ne to ^{58}Ni. Cross sections were measured for all fragment elements with charges greater than or equal to half the charge of the projectile. The results show that, over the energy and ion range investigated, the general decrease in cross section with decreasing fragment charge is strongly modified by the isospin of the projectile ion. Significant additional modifications of the cross sections due to the internal structure of the nucleus have also been seen. These include both pairing and shell effects. Differences in the cross sections due to the differing energies of the projectile are also considerable.

PACS number(s): 25.75.−q, 25.70.Mn, 98.70.Sa

I. INTRODUCTION

A long standing problem in the study of galactic cosmic rays (GCR's) is deducing the elemental and isotopic composition at the source from the observed abundances. A definitive determination of the source composition would lead to a better understanding of the nucleosynthesis processes and acceleration mechanisms occurring at the source(s). The GCR elemental and isotopic populations observed at Earth, however, are very likely to be appreciably different from those at the source, due to interactions of the cosmic-ray nuclei with the interstellar medium (ISM) during transport in the galaxy that result in nuclear fragmentation. Evaluating the effects that these interactions have had on the GCR composition requires values of the elemental and isotopic production cross sections, determined as a function of the energy, for all of the nuclear species that have significant abundances.

The number of cross sections required for such calculations of cosmic-ray transport is so large that it is virtually impossible to measure all of them; hence it has been necessary to develop various formalisms that attempt to predict values for those that have not been measured [1–5]. These formalisms have generally proved relatively unreliable, resulting in discrepancies, when compared with new measurements, that significantly exceed the accuracies of better than 10% that are necessary to address many of the questions of interest.

Many of the data used to develop the early predictions were obtained from experiments in which protons bombarded targets of various materials [2,6,7]. Cross sections for the production of specific unstable isotopes could then be determined by observing their decay. This led to the prediction formalism being derived from a relatively small number of cross sections. More recently [8–12] data from heavy-ion beams have been used to improve the predictions. This technique of using heavy-ion beams interacting in fixed targets has several advantages, the most important of which for this analysis is that since all of the heavy fragments ($Z \geqslant Z_{\text{projectile}}/2$) are observed the elemental and isotopic cross sections can be measured directly.

The Transport Collaboration, composed of researchers from eight institutions in Italy, France, and the U.S.A., was formed to study the problem of cosmic-ray transport, paying particular attention to the measurement of new cross sections. The main thrust of this paper is to report the measured elemental cross sections and to use them to examine the nuclear physics of fragmentation reactions, and to compare them with predicted cross sections. This may in turn provide some guidance as to how to improve cross section predictions.

Due to the sheer volume of data, and the complexity of the analysis, we are reporting the results of our program in a

*Current address: Lawrence Berkeley Laboratory, 1 Cyclotron Road, Berkeley, CA 94720.

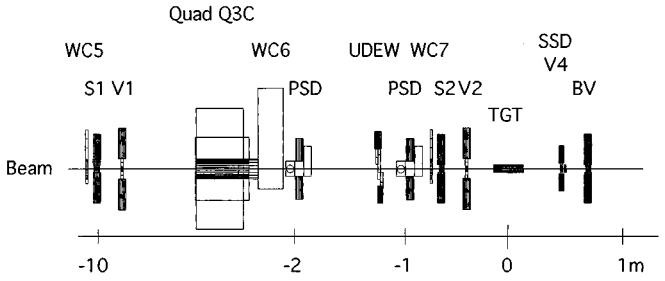

FIG. 1. The portion of the experimental setup upstream of the HISS magnet. The quad Q3C was a focusing magnet, and the wire chambers (WC's) were used to monitor the beam while it was being tuned.

series of papers. This paper concentrates on the elemental production cross sections, including relevant details of the experimental setup and acceptance and thick target corrections. A companion paper on the charge changing total cross sections has recently been published [13]. Isotopic production cross sections will be reported in future papers.

II. EXPERIMENTAL TECHNIQUE

The primary goal of these experiments was to identify fragment isotopes produced by various beams of incident nuclei interacting in a target of liquid hydrogen, and to obtain their production cross sections. Details of the complete set of detectors are discussed by Chen *et al.* [13] and Albergo *et al.* [14]. The experimental setup was employed for two runs which took place in April 1990 and 1991 using the HISS facility at the LBL Bevalac.

The projectiles and energies studied during the runs include ^{22}Ne at 377, 581, and 894 MeV/nucleon; ^{26}Mg at 371 and 576 MeV/nucleon; ^{32}S at 365, 571, and 770 MeV/nucleon; ^{36}Ar at 361, 546, and 765 MeV/nucleon; ^{40}Ar at 352 MeV/nucleon; ^{40}Ca at 357, 565, and 763 MeV/nucleon; ^{52}Cr at 343 MeV/nucleon; and ^{58}Ni at 338 MeV/nucleon. The energies listed are those at the center of the target.

The identification of the charges of the fragments used the portion of the apparatus shown in Fig. 1. This includes the upstream detectors, the target, and the charge measuring detectors immediately following the target. The HISS magnet and other detectors (not shown), which were necessary for mass identification, were not used in this analysis.

The detectors upstream of the target provide timing and vectoring information on the incoming beam particles, and monitor beam quality. The array of detectors included scintillators that gave timing and charge information, veto detectors that provided active collimation of the beam, and position sensitive detectors (PSD's) that allowed the determination of the vector of the beam projectile, on an event by event basis. There were slight differences for the 1990 run, but the general setup was the same except that the V4 detector was absent.

The trigger for the experiment was derived primarily from the upstream S1,V1, and S2,V2 detectors and the UDEW (up-down-east-west) detector. S1 and S2 were scintillators which provided timing information. S2 also provided charge information that was used to reject events in which the beam projectile had interacted upstream of the target. The three

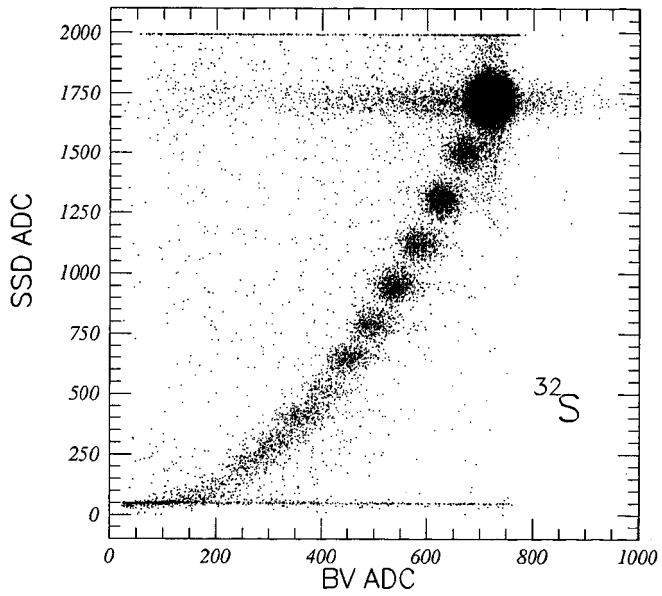

FIG. 2. A scatter plot of SSD ADC vs BV ADC for ^{32}S at 571 MeV/nucleon, with a BEAM trigger.

veto detectors, V1, V2, and UDEW, that provided active collimation were scintillators, V1 and V2 having circular apertures (1.0 and 2.54 cm in diameter, respectively), UDEW having an adjustable rectangular aperture. A special purpose electronic module was used for on-line pileup rejection. This was the updating one shot or UDOS, which used signals from S1 and V1.

There were two charge measuring detectors immediately following the target. The primary post-target charge measuring device was a 1 mm thick Si(Li) solid state detector (SSD) and the secondary detector was a 3 mm thick scintillator, the beam veto (BV). The V4 detector was a scintillator, with a 4.5 cm circular aperture, associated with the solid state detector, that was used to reject events in which the leading fragment missed the active area of the SSD. The basic trigger condition for data taking, designated BEAM, was $\text{BEAM} = (\text{S1}\cdot\overline{\text{V1}})\cdot(\text{S2}\cdot\overline{\text{V2}})\cdot\overline{\text{UDEW}}\cdot\overline{\text{V4}}\cdot\overline{\text{UDOS}}$.

For a large portion of the run time ($\approx$35%), the BV was used to eliminate from the trigger most ($>$90%) of the beam particles that did not interact in the target. A threshold on the signal from the BV, BVh, was set to eliminate events in which a particle with the same charge as the beam projectile struck the BV detector. An ''interaction'' trigger designated INT, $\text{INT} = \text{BEAM}\cdot\overline{\text{BVh}}$, was used for these runs. The rejection of events was based on the measured charge in the BV scintillator. This was done to increase the number of interactions recorded in the finite time available. The data taken with the INT trigger were normalized to the BEAM trigger data using the procedure described in Sec. III.

The target was liquid hydrogen (LH_2), approximately 0.25 g/cm^2 thick, contained between titanium windows a total of 0.18 g/cm^2 thick. The target-out (T0) data were taken using a ''mass dummy'' which contained titanium windows with the same total thickness as those on the LH_2 target. This is the equivalent of emptying the liquid hydrogen out of the target. The interaction rate for the mass dummy was on the order of half of that for the full target. The windows of the LH_2 target were permanently deformed during pressure testing; thus the

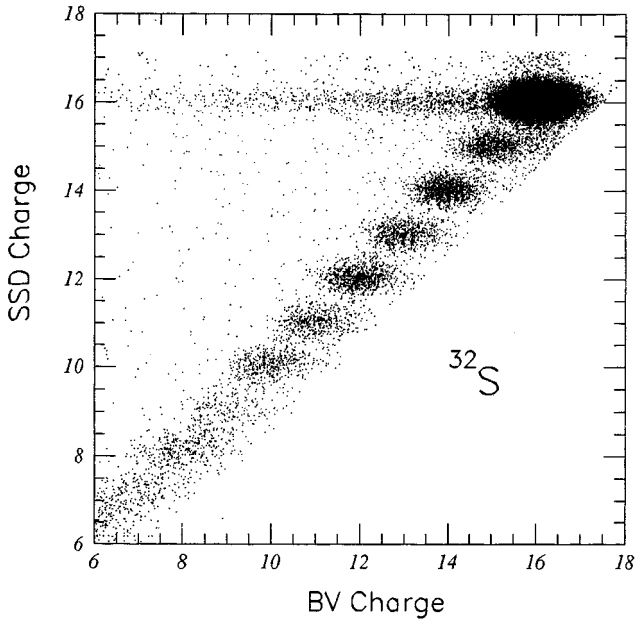

FIG. 3. A plot of the data shown in Fig. 2 displaying SSD charge vs BV charge. This plot shows the effect of the charge calibration, as well as the charge consistency cuts. The superior charge resolution of the SSD detector can be seen.

exact target thickness depended on where the projectile struck the target. For details of the target construction and thickness calculations see Albergo *et al.* [14], Engelage *et al.* [15], and Chen *et al.* [13].

Figure 2 shows a scatter plot of the raw analog-to-digital converter (ADC) response, with a BEAM trigger, of the two charge measuring detectors (BV and SSD) for ^{32}S projectiles with 571 MeV/nucleon at the target. The SSD had the quadratic response to the charge that is typical of such detectors, while scintillator saturation effects resulted in a linear dependence of the BV signal on charge. The procedure for extracting the charge began by applying independent charge calibrations to the two detectors. For the SSD, the calibration was $Z_{\mathrm{SSD}}=C_1\times(\mathrm{ADC_{SSD}})^{1/2}+C_2$. For the BV, $Z_{\mathrm{BV}}=C_3\times\mathrm{ADC_{BV}}+C_4$. Deviations from these functional forms could be as large as $0.1e$ for the lightest beam, ^{22}Ne. The four constants were determined separately for each ion-energy combination. The slight energy loss in the liquid hydrogen required different calibrations for the target-in and target-out data.

The fragment charge determination could be improved by combining the information from the BV and the SSD, depending on the results of an internal consistency test. The SSD showed much better charge resolution than the BV, but suffered from pileup effects due to the relatively long time constant of the SSD ($\sim 1\mu$s).

Figure 3 shows the same data as Fig. 2, but with the charge calibrations applied, and several cuts in effect. For the majority of the events, those lying close to the $Z_{\mathrm{BV}}=Z_{\mathrm{SSD}}$ line, the results from the two detectors were combined in a weighted average. A weighting of three to one in favor of the SSD gave the best final resolution, $Z=(Z_{\mathrm{BV}}+3Z_{\mathrm{SSD}})/4$. This weighting was used for all projectiles. The optimal weighting was determined empirically by varying the weights until the best resolution was obtained. The events in which the SSD

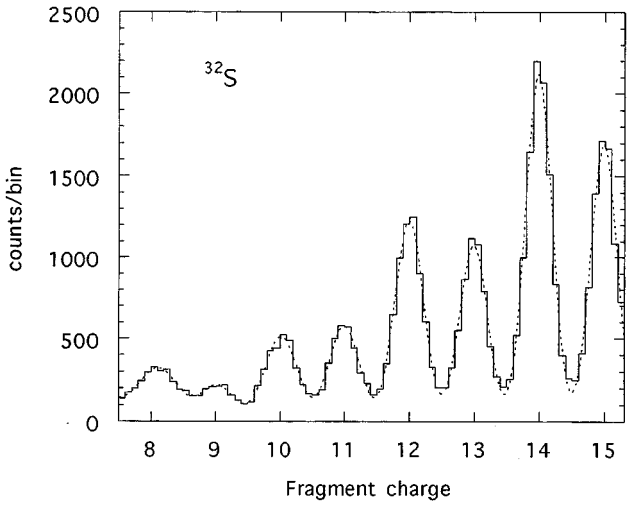

FIG. 4. A charge histogram of ^{32}S at 571 MeV/nucleon. The multiple Gaussian fit (dashed line) is included. This histogram is a sum of BEAM and INT trigger data; therefore the $Z=15$ peak is partially suppressed.

ADC overflows (the line along the top of Fig. 2) were removed by the cuts. For the events in which an interaction had taken place downstream of the target (the tail to the left of the $Z_{\mathrm{BV}}=Z_{\mathrm{SSD}}$ line in Fig. 3) we used $Z=Z_{\mathrm{SSD}}$. Those events in the tail to the right of the line of charge ''islands,'' in Fig. 2, were also removed by the cuts. These events were due to those particles which missed the active area of the relatively small SSD. The application of these cuts resulted in the necessity of including an acceptance correction for the fragments missing the SSD.

III. ANALYSIS

A. Cross section calculation

The populations for each fragment charge were extracted by fitting multiple Gaussians to the charge histograms. A typical charge spectrum with the appropriate fit is shown in Fig. 4. As there were two target positions, and two trigger settings, there were four types of data for each beam: LH_2 target BEAM trigger, LH_2 target INT trigger, T0 target BEAM trigger, T0 target INT trigger. In general $\sim$70–80% of the fragments were derived from the INT trigger data.

The target was thin, with the interaction rate in the liquid hydrogen varying from $\sim$4% to $\sim$9%, depending on the specific projectile. However, the contribution from the target container was quite large, making the total interaction rate for the target-in data $\sim$7% to $\sim$17%. Although this was a lower rate than that for most ''thick target'' experiments, it was necessary to consider, in some detail, the propagation of the projectiles and fragments through the target,

The production of fragment nuclei of a specific charge within the target can be described by the following differential equation:

$$\frac{dN_Z}{dx}=N_P(x)\sigma(P,Z)-N_Z(x)\sigma_{\mathrm{total}}(Z)+\sum_{j>Z}N_j(x)\sigma(j,Z). \tag{1}$$

The quantity x is the target thickness traversed, expressed in nuclei per mb (i.e., the thickness in g cm^{-2} multiplied by

the number of target nuclei per g and divided by the number of mb per cm^2) The subscript P indicates uninteracted projectiles. $N_P(x)$ is the number of projectiles at the position x, $N_Z(x)$ is the number of fragments of charge Z. The first term of Eq. (1) is the contribution to the number of fragments, of charge Z, from the projectile, and $\sigma(P,Z)$ is the elemental production partial cross section for charge Z; the quantity that we wish to measure. The second term is the loss of fragments to secondary interactions; $\sigma_{\text{total}}(Z)$ is the total charge changing cross section for the fragment. The third term is the contribution from secondary interactions of fragments with higher charge. The quantity $N_p(x)$ is derived from the known number of projectiles entering the target, N_P $[=N_P(0)]$, and can be derived from Eq. (1) by substituting P for Z and only including the loss term. The result is

$$N_P(x)=N_P(0)e^{-x\sigma_{\text{total}}(P)}, \tag{2}$$

where $\sigma_{\text{total}}(P)$ is the total charge changing cross section for the projectile.

When secondary interactions were neglected, the second and third terms of Eq. (1), the solution to Eq. (1) became

$$\frac{N_Z}{N_P}=\frac{\sigma(P,Z)}{\sigma_{\text{total}}(P)}\,(1-e^{-T\sigma_{\text{total}}(P)}), \tag{3}$$

where T is the total target thickness. For an infinitely thin target, Eq. (3) can be simplified by expanding the exponential and neglecting higher terms. This leads to a cross section of

$$\sigma(P,Z)=\frac{1}{T}\frac{N_Z}{N_P}. \tag{4}$$

The charge population values (N_Z) are the areas under the individual Gaussian peaks, with a correction for the instrument acceptance, V_Z. The population for a particular charge $N_Z=A_ZV_Z$, where A_Z is the number of particles derived from the multiple Gaussian fit to the charge histogram (Fig. 4) and V_Z is calculated for that particular charge (see Sec. III C).

The thick target calculation involved a numerical solution to Eq. (1), which is explained in detail in the Appendix. The principle is fairly simple; the target (both the LH_2 and ''background'' material, see the Appendix) was divided up into many thin slabs, and a sum was used to replace the integral that would otherwise be necessary to solve the equation. The slabs were sufficiently thin that the relationship in Eq. (4) could be used. The assumed values for the partial cross sections $\sigma(P,Z)$ were adjusted until the final number of fragments calculated matched the number observed. The initial estimates for these cross sections were essentially those determined with Eq. (4). The secondary cross sections were treated as fixed parameters.

There were two factors which made a somewhat more complicated technique necessary. The simpler of the two was the acceptance correction. Due to the physical size of the target the acceptance correction varied slightly depending on the depth in the target at which the interaction took place. This was accounted for by applying the acceptance correction separately for each slab. More difficult was the target-out correction. In most experiments when a thick target corection is applied the target-out correction is very small. In this experiment this was not the case and it was necessary to use a two-step procedure. First a thick target correction was run on the target-out data. The cross sections from this procedure were then used in the full target correction.

The final corrections to the thin target values varied significantly depending on the projectile and fragment. For fragments with small charge changes the correction significantly increased over the thin target value. The largest enhancements were on the order of 25–30 % for the highest charge fragments from ^{58}Ni, ranging down to 7–10 % for the high charge fragments of ^{22}Ne. These values are the ratio between the final thick target cross sections and the results of Eq. (4). This enhancement was due to the loss of fragments from the second term of Eq. (1), as well as the loss of projectiles described by Eq. (2). Each of these two effects accounts for roughly half of the enhancement. For these heavy fragments the third term of Eq. (1) was not particularly significant. For lighter fragments the third term of Eq. (1) became significant; in a few cases it was a major contribution to the number of fragments. This could result in the thick target cross section being lower than the thin target value. The details of the calculation are explained in the Appendix.

The determination of the cross sections for the Z_P-1 fragments presented a separate problem. The threshold on the BV output, BVh, used in the INT trigger was set to reject uninteracted beam nuclei yet minimize the loss of fragments. However, since some percentage of the Z_P-1 fragments were also rejected, the INT trigger data were unsuitable for extracting the Z_P-1 cross section. The possibility of the BVh cut affecting the Z_P-2 population was investigated, and found in the worst case to be less than 0.1%, and thus insignificant.

The charge populations used in the cross section calculations were derived from fits to a charge spectrum that combined both the INT and BEAM trigger data. The number of incoming projectiles for the BEAM data was known directly, but the number for the INT trigger data had to be derived from the BEAM trigger data by comparing the number of fragments in a portion of the charge spectrum, from $Z_P/2$ to Z_P-2, that was unaffected by the difference in the trigger logic. The charge populations could be reliably determined down to $Z_P/2$. The normalization factor R was the ratio of the populations in this range for the two triggers, S_{BEAM} and S_{INT}:

$$R^{\text{LH}_2}=\left(\frac{S^{\text{LH}_2}_{\text{BEAM}}}{S^{\text{LH}_2}_{\text{INT}}}\right) \tag{5}$$

where

$$S^{\text{LH}_2}_{\text{BEAM}}=\sum_{Z=Z_P/2}^{Z_P-2} N^{\text{LH}_2}_{Z,\text{BEAM}} \tag{6}$$

and

$$S^{\text{LH}_2}_{\text{INT}}=\sum_{Z=Z_P/2}^{Z_P-2} N^{\text{LH}_2}_{Z,\text{INT}}. \tag{7}$$

The total number of incoming projectiles for the sum of the INT and BEAM trigger data was

$$N_{\text{total}}^{\text{LH}_2}=N_{\text{BEAM}}^{\text{LH}_2}\left(1+\frac{S_{\text{INT}}^{\text{LH}_2}}{S_{\text{BEAM}}^{\text{LH}_2}}\right). \quad (8)$$

The interaction trigger also cuts out a percentage of the fragments with a charge change of 1, Z_P-1. As a result only the BEAM trigger data could be used to extract the cross sections for these fragments, which results in increased statistical uncertainties for these cross sections.

B. Calculation of uncertainties

The sources of uncertainty included counting statistics and fitting, acceptance calculations, the normalization of the INT trigger data, and biases introduced by the charge consistency cuts. The correction for the finite thickness of the target also involved some uncertainty. However, for the Z_P-1 cross sections the main source of uncertainty was in separating the Z_P-1 peak from the projectile peak. The problem was especially pronounced for the target-out data. It is primarily this difficulty, rather than the increased counting uncertainties, that explains the rather large uncertainties for the Z_P-1 cross sections, as well as why they tended to be largest for the heaviest beam projectiles.

For the final uncertainty calculation, the thick target calculation was treated as a simple multiplicative correction. The uncertainties of the thin target cross section were first calculated using Eq. (4) with a background subtraction:

$$\sigma(P,Z)=\frac{1}{T}\left[\frac{N_Z^{\text{LH}_2}}{N_P^{\text{LH}_2}}-\frac{N_Z^{\text{T0}}}{N_P^{\text{T0}}}\right]. \quad (9)$$

The uncertainty for this initial cross section was determined using

$$[\Delta\sigma(P,Z)]^2=\left(\frac{\Delta T}{T}\,\sigma(P,Z)\right)^2+\left(\frac{\Delta N_Z^{\text{LH}_2}}{TN_P^{\text{LH}_2}}\right)^2+\left(\frac{\Delta N_P^{\text{LH}_2}N_Z^{\text{LH}_2}}{T(N_P^{\text{LH}_2})^2}\right)^2+\left(\frac{\Delta N_Z^{\text{T0}}}{TN_P^{\text{T0}}}\right)^2+\left(\frac{\Delta N_P^{\text{T0}}N_Z^{\text{T0}}}{T(N_P^{\text{T0}})^2}\right)^2. \quad (10)$$

This uncertainty was combined with that determined for the thick target correction. The thick target uncertainty was determined using a Monte Carlo technique, which determined the uncertainties due to the secondary cross sections, which were not known precisely. This technique is described in detail in the Appendix. In general, the thick target correction was not a major source of uncertainty; typically the fractional uncertainty was only increased by a few percent. In a few cases the uncertainty was increased by as much as 15% of its value.

The final uncertainties were determined by formulating the thick target correction as $\sigma(P,Z)=C\sigma_{\text{thin}}$. The uncertainty could then be calculated using the formula

$$\Delta\sigma(P,Z)=\sigma(P,Z)\sqrt{(\Delta C/C)^2+(\Delta\sigma_{\text{thin}}/\sigma_{\text{thin}})^2}, \quad (11)$$

where the value of ΔC is the uncertainty in the correction calculated using the Monte Carlo technique, $\sigma(P,Z)$ is the final cross section, and the values with the subscript "thin" are the cross sections and uncertainties from Eqs. (9) and (10), respectively.

C. Instrument acceptance

The acceptance was defined, for the 1991 runs, by the V4 and SSD, while for 1990 it was defined by the SSD alone, as the V4 detector was only in place for the April 1991 run. The appropriate acceptance, and the associated uncertainties, were calculated using a Monte Carlo code which models the scattering from V2 through the target to the V4 and SSD detectors. The V2 detector was used as it defined the x-y limits of the beam immediately upstream of the target. Vectoring information from the PSD's was also used. The threshold on the V4 detector was set to reject events in which a fragment with charge $>\approx 0.25Z_P$ struck the detector. This meant that leading fragments striking the V4 were rejected; however, the detector was not sensitive to the most common secondary fragments, i.e., protons and α particles.

The scattering in the target was determined using a computer code which included a Goldhaber [16] approximation with an added Coulomb scattering term. The scattering produces a distribution that depends on the mass of the fragment. To get a correction for a given fragment charge a weighted average of the isotopes of that charge was used. The weights were provided by a cross section prediction code supplied by Webber, Kish, and Schrier [1]. The sensitivity of the final correction to variations in the isotope distribution was investigated and found to be much less than other sources of uncertainty.

The magnitude of this acceptance correction depended on several factors: the mass of the beam, the beam energy, the mass of the fragment, the x-y distribution of beam projectiles (i.e., the beam tune), and the locations of the various detectors. For the majority of the fragments the correction was quite small, 0–3 %. The correction only became significant for the combination of light beam, low energy, and light fragment. The uncertainties in the correction were typically on the order of 30% of the size of the correction. As a relatively extreme example, the correction applied to the nitrogen ($Z=7$) fragments produced by 377 MeV/nucleon ^{22}Ne projectiles was 1.080 ± 0.023. It was found during the calculations that the dominant source of uncertainty in the correction was the uncertainty in the physical positions of the detectors as determined by the survey performed after each run.

IV. RESULTS AND INTERPRETATION

The cross sections that we report here, listed in Table I, can give us some insight into the physics of fragmentation reactions in the range of projectile mass and energy studied. For much heavier projectiles, a simple exponential dependence of the cross sections on the amount of charge lost is seen ($\sigma\approx ae^{-b\Delta Z}$) [12]. For projectiles in the mass range that we have used, the situation is more complex. Perhaps the most important observation is that the internal nuclear structure of the projectile and the fragment have a significant

TABLE I. Elemental production cross sections.

^{22}Ne $E=377$ MeV/nucleon			^{22}Ne $E=581$ MeV/nucleon			^{22}Ne $E=894$ MeV/nucleon		
Z_f	σ	$\delta\sigma$	Z_f	σ	$\delta\sigma$	Z_f	σ	$\delta\sigma$
9	81.2	5.2	9	79.1	5.0	9	83.6	4.8
8	69.5	2.5	8	66.9	2.3	8	65.2	2.0
7	51.6	2.2	7	56.1	2.3	7	54.1	1.8
6	42.2	3.1	6	48.3	2.9	6	48.4	2.2
5	14.9	2.7	5	22.9	3.9	5	25.9	3.4

^{26}Mg $E=371$ MeV/nucleon			^{26}Mg $E=576$ MeV/nucleon		
Z_f	σ	$\delta\sigma$	Z_f	σ	$\delta\sigma$
11	106.2	8.4	11	99.3	9.2
10	81.0	4.4	10	75.3	3.7
9	34.4	2.5	9	42.2	2.4
8	39.2	3.3	8	53.0	3.5
7	29.5	2.9	7	38.1	4.6
6	20.1	2.8	6	45.7	7.1

^{32}S $E=365$ MEV/nucleon			^{32}S $E=571$ MeV/nucleon			^{32}S $E=770$ MeV/nucleon		
Z_f	σ	$\delta\sigma$	Z_f	σ	$\delta\sigma$	Z_f	σ	$\delta\sigma$
15	75.0	8.6	15	77.3	10.0	15	79.9	13.7
14	111.3	4.9	14	112.2	3.8	14	103.5	3.9
13	58.3	3.2	13	62.8	2.6	13	56.6	2.7
12	63.7	3.6	12	75.4	2.9	12	68.8	2.9
11	30.7	2.6	11	36.5	1.9	11	36.4	2.2
10	27.6	2.7	10	36.0	2.0	10	38.8	2.4
9	9.8	2.2	9	15.0	1.8	9	16.7	2.9
8	16.5	3.1	8	27.2	3.4	8	27.4	4.3

^{36}Ar $E=361$ MeV/nucleon			^{36}Ar $E=546$ MeV/nucleon			^{36}Ar $E=765$ MeV/nucleon		
Z_f	σ	$\delta\sigma$	Z_f	σ	$\delta\sigma$	Z_f	σ	$\delta\sigma$
17	77.4	20.8	17	69.1	9.5	17	71.5	10.3
16	103.9	5.3	16	95.0	3.5	16	96.5	5.2
15	64.6	3.6	15	57.3	2.4	15	53.6	3.4
14	92.6	4.9	14	88.7	3.1	14	95.3	4.5
13	44.0	2.8	13	43.3	2.1	13	47.3	2.9
12	40.1	2.8	12	45.1	2.2	12	55.1	3.3
11	19.7	1.9	11	21.4	1.7	11	29.9	2.4
10	15.5	2.1	10	19.5	2.2	10	24.4	2.6
9	8.6	2.1	9	5.3	4.8	9	10.0	4.9

^{40}Ar $E=352$ MeV/nucleon		
Z_f	σ	$\delta\sigma$
17	146.0	10.7
16	109.0	4.2
15	70.4	3.0
14	62.0	2.9
13	29.3	1.9
12	21.2	1.8
11	9.3	1.3
10	5.8	1.7
9	2.6	1.7

TABLE I. (*Continued*).

^{40}Ca $E=357$ MeV/nucleon			^{40}Ca $E=565$ MeV/nucleon			^{40}Ca $E=763$ MeV/nucleon		
Z_f	σ	$\delta\sigma$	Z_f	σ	$\delta\sigma$	Z_f	σ	$\delta\sigma$
19	70.5	15.8	19	63.7	10.3	19	88.3	14.5
18	108.0	3.8	18	99.6	3.2	18	98.9	2.9
17	66.0	2.8	17	61.0	2.3	17	61.9	2.2
16	85.3	3.3	16	83.8	2.9	16	80.7	2.5
15	45.9	2.5	15	47.3	2.1	15	48.8	1.8
14	50.7	2.8	14	63.9	2.9	14	69.1	2.1
13	25.1	2.0	13	31.8	1.8	13	36.3	1.6
12	17.9	2.0	12	29.9	2.0	12	36.8	1.7
11	6.7	1.6	11	13.4	1.5	11	18.8	1.6
10	5.8	1.9	10	10.8	2.5	10	15.8	2.2

^{52}Cr $E=343$ MeV/nucleon			^{58}Ni $E=338$ MeV/nucleon		
Z_f	σ	$\delta\sigma$	Z_f	σ	$\delta\sigma$
23	174.0	24.0	27	115.3	23.6
22	126.4	4.8	26	140.6	7.5
21	79.7	3.3	25	109.7	5.9
20	64.6	2.8	24	104.8	5.6
19	35.3	2.0	23	61.5	4.7
18	26.1	1.8	22	52.0	3.7
17	12.8	1.7	21	31.3	3.1
16	9.7	1.6	20	16.2	4.0
15	5.7	1.3	19	10.0	3.0
14	1.9	1.5	18	4.3	2.8
13	1.1	−1.1,+1.3	17	2.5	2.0
12	0.0	−0.0,+1.4	16	1.7	−1.7,+2.3
			15	0.0	−0.0,+2.2
			14	0.0	−0.0,+1.7

effect on the cross sections. In all, we see three different factors affecting the cross sections; the internal nuclear structure of the fragment, the isospin of the projectile ($T_z=2Z-A$), and the interaction energy. These three factors interact in a rather complex manner.

The structure of the fragment can be seen most clearly in the strong odd-even variation shown in Fig. 5. We interpret this variation as being due to the pairing force between the protons in the fragment [17]. This interpretation is supported by the relative magnitudes of the pairing interaction, a few MeV per pair, and the total binding energy per nucleon, roughly 8 MeV/nucleon in the mass range in question.

A similar, but less dramatic, effect is due to the shell structure of the fragment. A close examination of the cross sections reported here and elsewhere shows effects due to the closed shell at $Z=8$ and the closed $d_{5/2}$ subshell at $Z=14$. Since we are considering elemental cross sections, only the proton shell structure is visible. The effect of the sub-shell at $Z=14$ can be seen most clearly in Fig. 6, which shows three different energies of ^{40}Ar. The two higher energies are taken from Webber, Kish, and Schrier [8]. An enhanced production of silicon ($Z=14$) is observed at all energies, but is more pronounced at higher energies. Another indication of this behavior can be seen in Fig. 7(a). The general trend of the cross sections would indicate that the $\Delta Z=8$ cross section for oxygen fragments from ^{32}S projectiles should be significantly less than that for neon fragments from ^{36}Ar or magnesium fragments from ^{40}Ca; instead, it is approximately the same. Presumably this is due to the closed proton shell for oxygen ($Z=8$).

We have found that the general trend of the elemental cross sections for a specific projectile depends most significantly on the isospin of the beam projectile. This can be seen clearly in Figs. 7(a) and 7(b), which compare the cross sections from three projectiles with isospin of zero (a) to two projectiles with $T_z=-2$ (b). The projectiles with $T_z=0$ all show a dramatic odd-even variation of the cross sections. The $T_z=-2$ projectiles, which have four more neutrons than protons, show no odd-even effect. In addition there is a clear difference in the rate at which the cross sections decrease with increasing charge change. The $T_z=-2$ projectiles show a rapid, roughly exponential, dropoff. In contrast the $T_Z=0$ projectiles show a roughly linear decrease. The behavior of the $T_z=-2$ projectiles is similar to the roughly exponential dependence that is seen for much heavier projectiles regardless of their isospin [12]. It is apparent that the presence of excess neutrons suppresses the odd-even effect. The presence of excess neutrons, apparently, mitigates the effect of the proton pairing interaction which is presumed to cause the odd-even effect. The isospin of the projectile has also been seen, in other work, to affect the total charge changing cross section [18].

The behavior of the $T_z=-1$ projectiles is somewhat difficult to characterize. This is due in part to the fact that only

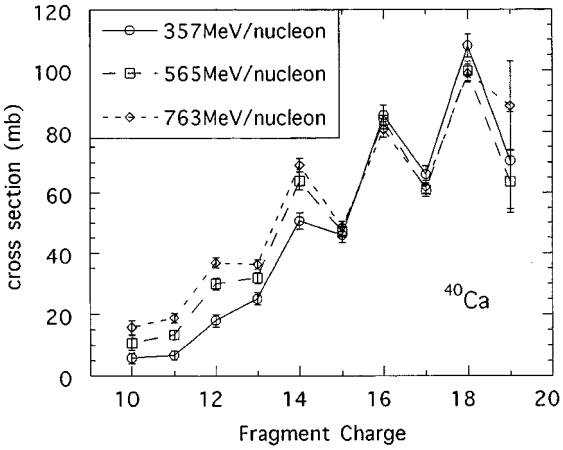

FIG. 5. Elemental production cross sections vs fragment charge for three projectile energies of ^{40}Ca. The strong odd-even effect that is typical for $T_z=0$ projectiles is clear. The effect of projectile energy is to increase the cross sections for the low charge fragments.

the lightest (^{22}Ne and ^{26}Mg) and heaviest (^{58}Ni) of the projectiles that we employed had an isospin of -1. The cross sections from nickel seem to show an intermediate behavior when compared to the $T_z=0$ and -2 projectiles. There is a reduced odd-even effect from that of the $T_z=0$ projectiles, and the decrease in the cross sections is less rapid than for the $T_z=-2$ projectiles.

The energy of the beam projectile also influences the cross sections and the odd-even effect. As can be seen in Fig. 5, increasing the projectile energy causes an increase in the cross sections for large charge changes. Previous work [8] has shown a decrease in the cross sections for small charge changes with increasing energy. There are some indications of this for some projectiles in our data, specifically ^{36}Ar. Also, at large charge changes, the odd-even effect is more pronounced for higher energies. As can be seen in Fig. 6, increasing the projectile energy also makes effects due to the shell structure of the fragment more pronounced. This is a somewhat counterintuitive result. It would seem more likely

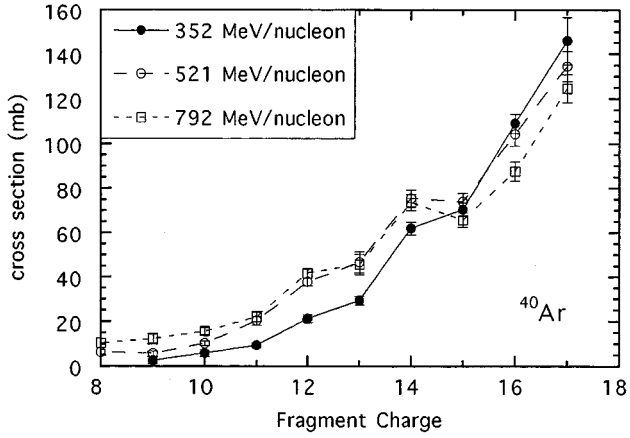

FIG. 6. Elemental production cross sections vs fragment charge for three projectile energies of ^{40}Ar. The two higher energies (open symbols) are from Webber, Kish, and Schrier [8]. The key feature is the enhancement at $Z=14$.

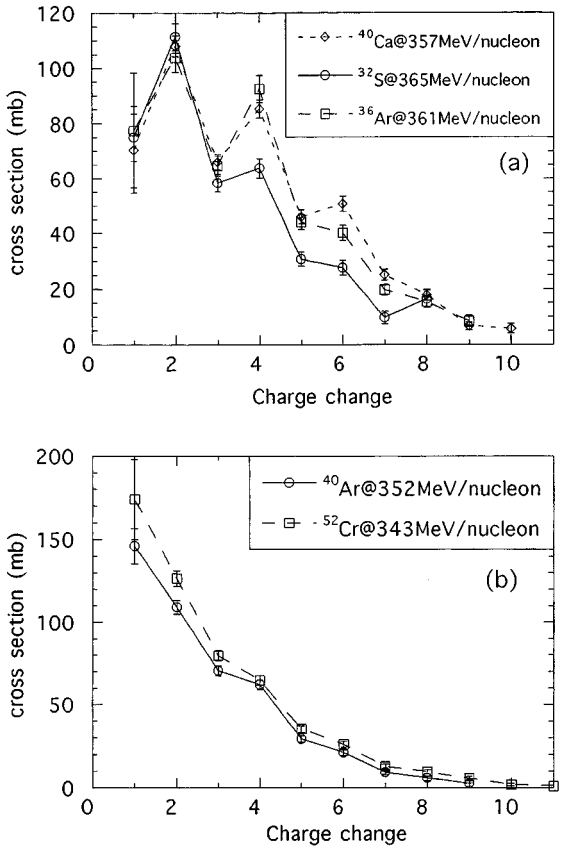

FIG. 7. Elemental production cross sections vs fragment charge for three projectiles with $T_z=0$ and roughly the same energy (a) are compared to two projectiles with $T_z=-2$ (b). The strong effect of the isospin of the projectile can be clearly seen. The difference between ^{36}Ar and ^{40}Ar is quite dramatic.

that an increase in energy would "wash out" any structural or pairing effects, rather than accentuating them.

As the purpose of this experiment is to explore cross sections of astrophysical significance, we compare our results to the two main computer codes that are used by astrophysicists to predict cross sections that have not been measured. The first is the long extant, and much modified, semiempirical code by Silberberg and Tsao [3]. This is mainly based on cross sections obtained from proton bombardment experiments. More recently Webber, Kish, and Schrier [1] have introduced a parametric representation, based on cross sections from an experiment which also identifies individual fragments [8–10]. Both codes calculate the isotopic production cross sections; hence the values used here for comparison are simply the sum of the isotopic cross sections for each element.

Figure 8 shows a direct comparison of the two predictions to the cross sections listed in Table I. The diagonal line is $\sigma_{\text{predicted}}=\sigma_{\text{measured}}$ and is included to guide the eye. Both predictive techniques do reasonably well, although the Webber *et al.* predictions seem to be better for the larger cross sections while the Silberberg and Tsao predictions are better for the smallest cross sections. Figure 9 shows histograms of the difference between the predicted and measured cross sections, divided by the measured cross section. Neither technique consistently meets the 10% accuracy that is desired for use in propagation calculations. However, since in some

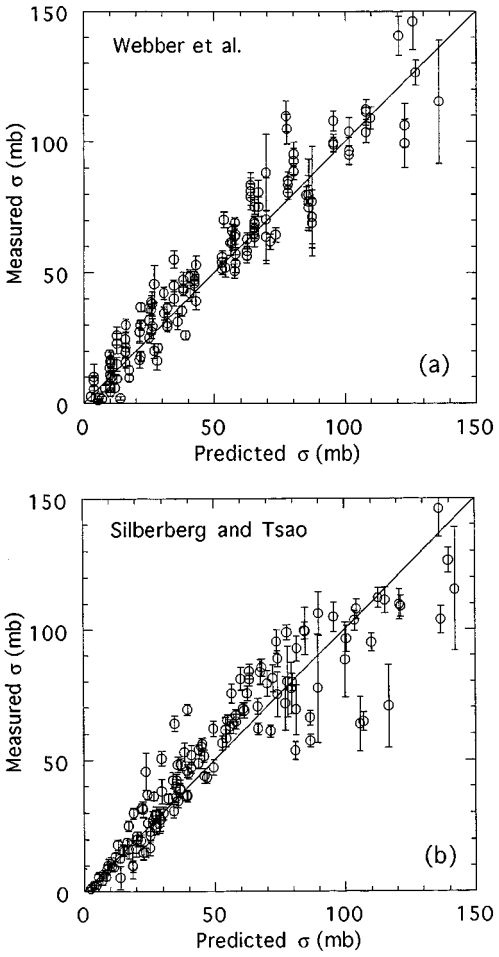

FIG. 8. Plots of measured vs predicted elemental cross sections for the techniques of Webber, Kish, and Schrier [1] (a) and Silberberg and Tsao [3] (b). The Webber *et al.* predictions are generally superior to those of Silberberg and Tsao for larger cross sections.

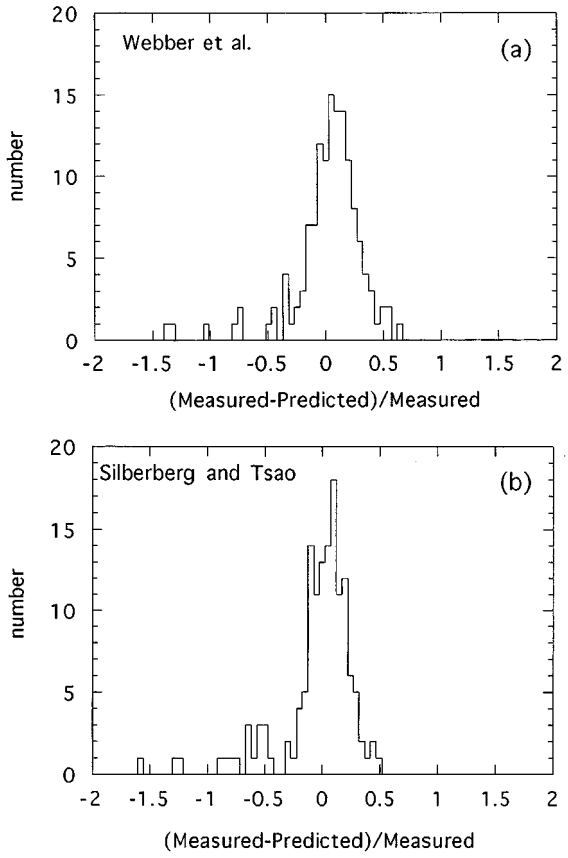

FIG. 9. Histograms of the fractional difference between the measured and predicted cross sections for Webber, Kish, and Schrier [1] (a) and Silberberg and Tsao [3] (b).

cases the experimental uncertainty is greater than 10% this is not in all cases a definitive judgment. It should be noted that the parametric fits used by Webber *et al.* were based on a data set that included several runs that were for the same projectiles and similar energies to several of our runs.

V. CONCLUSIONS

For the range of projectile mass and energy under consideration, $A=22-58$, $E\approx 300-900$ MeV/nucleon, we can make the following statements. The most important quantity in determining the overall behavior of the elemental production cross sections of a particular projectile nucleus is the isospin of that nucleus. Isospin is more important than either charge or mass. Significant nuclear structure effects have been seen. The structure effects are modified by both the energy and isospin of the projectile. The cross sections for relatively large charge changes are dependent on the energy of the projectile, with higher energies yielding larger cross sections. Any successful technique for predicting cross sections will have to explicitly take account of the effects due to isospin and nuclear structure.

ACKNOWLEDGMENTS

The Collaboration thanks the LBL Bevalac staff for their support during the experiment. Thanks are also due to B. Nilsen, I. Flores, S. Ko, C. Kuo, and J. Mazotta. Work supported at Louisiana State University by NASA under Grant No. NAGW-1526 and by DOE under Grant No. DE-FG05-ER 40147; at University of California, Berkeley by NASA under Grant No. NGR 05-003-513; at University of Minnesota by NASA under Grant No. NAGW-2004; at Lawrence Berkeley Laboratory in part by NASA under Grant No. L14230C; at New Mexico State University by NASA under Grant No. NAGW-3022; and at Università di Catania by INFN, Italy.

APPENDIX

In order to model the propagation through the target a somewhat simplified setup was considered. It was in principle necessary to consider all of the mass between the last detector before the target, S2, and the first detector after the target, SSD. The ''background'' was all of this material excluding the liquid hydrogen. Although several materials were present, the dominant contribution, in terms of interactions, came from the titanium windows. In the computer model it was assumed that all of the background was composed of titanium and concentrated immediately in front of and behind the liquid hydrogen. The other materials were not ig-

nored, rather they were ''replaced'' in the model by the amount of titanium which would yield the same number of interactions. The mass dummy data were used to calculate the interaction rate in the background and the results were applied to the LH_2 target data.

The production of specific fragment nuclei within the target is described by Eqs. (1) and (2) in the main text. When performing a numerical solution to Eq. (1) the appropriate equation was

$$N_Z(i)=A(Z,i)N_P(i-1)\Delta x\sigma(P,Z)-N_Z(i-1)\Delta x\sigma_{\text{total}}(Z)$$
$$+A(Z,i)\sum_{j>Z}N_j(i-1)\Delta x\sigma(j,Z). \quad \text{(A1)}$$

The quantity $N_P(i)$ was determined using the relation

$$N_P(i)=N_P(i-1)[1-\Delta x\sigma_{\text{total}}(P)] \quad \text{(A2)}$$

where $N_P(0)$ was the known number of projectiles entering the target. Here Δx is the thickness of the slab and $A(Z,i)$ was the appropriate acceptance correction for the charge and slab. It was not precisely correct to apply the same value to the secondary interactions as to the primaries; however, the introduced uncertainty was minuscule. For the mass dummy there were only two acceptance values, one for the first 50 slabs, and one for the last 50. This was due to the concentration of the mass in the background just before and after the hydrogen. The acceptance correction for the hydrogen slabs was varied linearly between these two values. Typically, the difference between $A(Z,1)$ and $A(Z,100)$ was on the order of 5%.

$$A(Z,i)=A(Z,1), \quad i\leqslant 50, \quad \text{mass dummy},$$
$$A(Z,i)=A(Z,100), \quad i>50, \quad \text{mass dummy},$$
$$A(Z,i)=A(Z,1)+(i-1)[A(Z,100)-A(Z,1)]/100, \quad LH_2. \quad \text{(A3)}$$

The quantities $\sigma(P,Z)$ were varied until the final number of fragments, $N_Z(100)$, matched that observed for the mass dummy data. It was the quantity $N_Z(100)/N_P(0)$ that was compared to the measured N_Z/N_P.

The cross sections for the mass dummy were then held fixed and the process was repeated for the full target. The beam was propagated through 50 slabs of background, then 100 slabs of hydrogen, then the remaining 50 slabs of background.

The values adopted for the secondary elemental cross sections were derived from isotopic cross sections predicted by Webber *et al.* The secondary cross sections were held in an array $\sigma(Z_1,Z_2)$. These were determined separately for each projectile, and consisted of the sum of isotopic cross sections for Z_2, with a weighted average over the isotopes of Z_1:

$$\sigma(Z_1,Z_2)$$
$$=\left(\frac{1}{\Sigma_{A_1}W(Z_1A_1)}\right)\sum_{A_1}\left[W(Z_1A_1)\sum_{A_2}\sigma(Z_1A_1,Z_2A_2)\right]. \quad \text{(A4)}$$

The weights W were the predicted cross sections $\sigma(Z_PA_P,Z_1A_1)$. The secondary total cross sections for each fragment isotope were determined using the formula [Chen *et al.* [13], Eq. (12)].

$$\sigma_{\text{total}}(A)=\pi r_0^2\left[A^{1/3}-\left(\frac{\lambda}{2r_0}\right)\frac{1}{A^{1/3}}\right]^2. \quad \text{(A5)}$$

Here A was the mass of the fragment, λ was an energy dependent parameter whose values are listed in Ref. [13] Table V, and r_0 is 1.35 fm. The secondary cross section for a given charge was determined by performing a weighted average over the isotopes, using predicted isotopic cross sections [1] as weights. They were then normalized to the measured total cross section using the value $N=\sigma_m(A_P)/\sigma_p(A_P)$, where $\sigma_m(A_P)$ was the measured total and $\sigma_p(A_P)$ was the predicted total cross section using the weighted average of the results from Eq. (4).

The secondary cross sections for the mass dummy were handled slightly differently than those for the LH_2. Since the quantity of interest was the number of fragments created or destroyed, the ''cross sections'' for the mass dummy (and LH_2 background) were determined and used as fractions. This eliminated the necessity of determining a ''target thickness'' for the mass dummy. The secondary elemental cross sections were derived from Webber, Kish, and Schrier [1] predictions for hydrogen by normalizing them with the ratio of the respective total cross sections. The predicted target-out total cross sections were determined from [Chen *et al.* [13], Eq. (11)]

$$\sigma_{\text{total}}(A_P)=\pi r_0^2(A_T^{1/3}+A_P^{1/3}-b)^2. \quad \text{(A6)}$$

Here the overlap parameter b was 0.97 for beam energies less than 400 MeV/nucleon and 0.83 otherwise. The value A_T was chosen to be 48 as titanium was the main component of the mass dummy. A weighted average and normalization procedure similar to that for the LH_2 was then performed. The main difference was that the mass dummy secondary total cross sections were normalized to the percentage interactions of the beam as listed in Chen *et al.* [13], Table III.

The procedure for determining the thick target cross sections was a two-step iterative approach. A set of initial cross sections was used to propagate a number of beam particles through the target. This was done by dividing the target into 100 slabs and doing a simple thin target calculation for each. The resulting number of fragments was then compared to the measured values. The initial values of the cross sections were then adjusted until the calculated number of each species of fragment matched the measured number.

The uncertainties were calculated using a Monte Carlo technique. This was done by randomly varying the secondary cross sections and repeating the above calculation. The calculation was repeated 100 times with different sets of secondary cross sections, and the rms deviation of the final correction was taken as the uncertainty. This assumed a 10% uncertainty for the secondary total cross sections, and a 50% uncertainty for the secondary elemental cross sections. These numbers were chosen to overestimate, rather than underestimate, the final uncertainties.

[1] W. R. Webber, J. C. Kish, and D. A. Schrier, Phys. Rev. C **41**, 566 (1990).
[2] M. Garcia-Munoz, J. A. Simpson, T. G. Guzik, J. P. Wefel, and S. H. Margolis, Astrophys. J. Suppl. Ser. **64**, 269 (1987).
[3] R. Silberberg and C. H. Tsao, in *Proceedings of the 20th International Cosmic Ray Conference*, Moscow, 1987, edited by V. A. Kozyarivsky, A. S. Linvansky, T. I. Tulupova, A. L. Tsyabuk, A. V. Voevodsky, and N. S. Volgemut (Nauka, Moscow, 1987), Vol. 2, p. 133.
[4] C. H. Tsao, R. Silberberg, A. F. Barghouty, L. Sihver, and T. Kanai, Phys. Rev. C **47**, 1257 (1993).
[5] L. Sihver, C. H. Tsao, R. Silberberg, T. Kanai, and A. F. Barghouty, Phys. Rev. C **47**, 1225 (1993).
[6] G. M. Raisbeck and F. Yiou, in *Spallation Nuclear Reactions and Their Applications*, edited by B. S. P. Shen and M. Merker (Reidel, Dordrecht, 1975), p. 83.
[7] T. G. Guzik, in *Particle Astrophysics: The NASA Cosmic Ray Program for the 1990s, and Beyond*, edited by W. V. Jones, F. J. Kerr, and J. F. Ormes, AIP Conf. Proc. No. 203 (AIP, New York, 1990), p. 275.
[8] W. R. Webber, J. C. Kish, and D. A. Schrier, Phys. Rev. C **41**, 520 (1990).
[9] W. R. Webber, J. C. Kish, and D. A. Schrier, Phys. Rev. C **41**, 533 (1990).
[10] W. R. Webber, J. C. Kish, and D. A. Schrier, Phys. Rev. C **41**, 547 (1990).
[11] G. D. Westfall, L. W. Wilson, P. J. Lindstrom, H. J. Crawford, D. E. Greiner, and H. H. Heckman, Phys. Rev. C **19**, 1309 (1979).
[12] W. R. Binns, T. L. Garrard, M. H. Isreal, M. P. Kertzmann, J. Klarmann, E. C. Stone, and C. J. Waddington, Phys. Rev. C **36**, 1870 (1987).
[13] C-X. Chen, S. Albergo, Z. Caccia, S. Costa, H. J. Crawford, M. Cronqvist, J. Engelage, P. Ferrando, R. Fonte, L. Greiner, T. G. Guzik, A. Insolia, F. C. Jones, C. N. Knott, S. Ko, C. Kuo, P. J. Lindstrom, J. Mazotta, J. W. Mitchell, R. Potenza, J. Romanski, G. V. Russo, A. Soutoul, O. Testard, C. E. Tull, C. Tuvé, C. J. Waddington, W. R. Webber, J. P. Wefel, and X. Zhang, Phys. Rev. C **49**, 3200 (1994).
[14] S. Albergo, Z. Caccia, C-X. Chen, S. Costa, H. J. Crawford, M. Cronqvist, J. Engelage, P. Ferrando, R. Fonte, L. Greiner, T. G. Guzik, A. Insolia, F. C. Jones, C. N. Knott, S. Ko, C. Kuo, P. J. Lindstrom, J. Mazotta, J. W. Mitchell, R. Potenza, J. Romanski, G. V. Russo, A. Soutoul, O. Testard, C. E. Tull, C. Tuvé, C. J. Waddington, W. R. Webber, J. P. Wefel, and X. Zhang, Nucl. Instrum. Methods (submitted).
[15] J. Engelage, S. Albergo, C-X. Chen, S. Costa, H. J. Crawford, P. Ferrando, L. Greiner, T. G. Guzik, F. C. Jones, C. N. Knott, S. Ko, C. Kuo, P. J. Lindstrom, U. Lynen, J. Mazotta, J. W. Mitchell, W. F. J. Mueller, D. Olson, R. Potenza, A. Soutoul, T. J. M. Symons, O. Testard, C. E. Tull, C. Tuvé, C. J. Waddington, W. R. Webber, J. P. Wefel, and H. H. Wieman, in *Proceedings of the 22nd International Cosmic Ray Conference*, Dublin, 1991, edited by M. Cawley, L. O'C. Drury, D. J. Fegan, D. O'Sullivan, N. A. Porter, J. J. Quenby, and A. A. Watsen (Dublin Institute for Advanced Studies, Dublin, 1991), Vol. 2, p. 531.
[16] A. S. Goldhaber, Phys. Lett. **53B**, 306 (1974).
[17] W. D. Myers and W. J. Swiatecki, Nucl. Phys. **81**, 1 (1966).
[18] T. Brohm, H.-G. Clerc, M. Dornik, M. Fauerbach, J.-J. Gaimard, A. Grewe, E. Hanelt, B. Voss, Ch. Ziegler, B. Blank, R. Del Moral, J.-P. Dufour, L. Faux, C. Marchand, M. S. Pravikoff, K.-H. Schmidt, H. Geissel, G. Münzenberg, F. Nickel, M. Pfützner, E. Roeckl, I. Schall, K. Sümmerer, D. J. Vieira, and M. Weber, Nucl. Phys. **A585**, 565 (1995).
[19] J. R. Letaw, R. Silberberg, and C. H. Tsao, Astrophys. J. Suppl. Ser. **51**, 271 (1983).
[20] J. Engelage, M. E. Baumgartner, E. Beleal, B. L. Berman, F. Bieser, F. P. Brady, M. Bronson, H. J. Crawford, I. Flores, D. E. Greiner, L. Greiner, O. Hashimoto, G. Igo, S. Kadota, P. N. Kirk, P. J. Lindstrom, C. McParland, S. Nagamiya, D. L. Olson, J. Porter, J. L. Romero, C. L. Ruiz, T. J. M. Symons, I. Tanihata, R. Wada, M. L. Webb, J. Yamada, and H. Yee, Nucl. Instrum. Methods Phys. Res. Sect. A **277**, 431 (1989).
[21] S. Albergo, S. Costa, M. Mazzeo, D. Nicotra, G. Poli, R. Potenza, C. Tuvé, H. J. Crawford, and I. Flores, Nucl. Instrum. Methods Phys. Res. Sect. A **311**, 280 (1992).
[22] B. S. Nilsen, Ph.D. thesis, University of Minnesota, 1994.
[23] H. C. Bradt and B. Peters, Phys. Rev. **77**, 54 (1950).